Structure, Heat Capacity, and High-Temperature Thermal Properties of $Yb_{14}Mn_{1-x}Al_xSb_{11}$

Catherine A. Cox,[†] Eric S. Toberer,[‡] Andrey A. Levchenko,[§,||] Shawna R. Brown,[†] G. Jeffrey Snyder,[‡] Alexandra Navrotsky,[§] and Susan M. Kauzlarich*,[†]

Department of Chemistry, University of California, One Shields Avenue, Davis, California 95616, Peter A. Rock Thermochemistry Laboratory and NEAT ORU, University of California, One Shields Avenue, Davis, California 95616, and California Institute of Technology, 1200 California Boulevard, Pasadena, California 91125

Received December 2, 2008. Revised Manuscript Received January 21, 2009

A series of compounds, $Yb_{14}Mn_{1-x}Al_xSb_{11}$ with ($0 < x < 1$), was prepared via Sn flux and the structures investigated. Single-crystal X-ray diffraction reveals that the volume of the unit cell increases with increasing Al content. Bond-distance changes are less than 2% and the increase in volume of the unit cell is associated with the decreasing distortion of the tetrahedron with increasing Al content. The specific heat, C_p, was measured from 300 to 1100 K. The measured C_p for these compounds is 19% higher than the Dulong-Petit value at the peak zT temperature (1223 K). These measured values permit a recalculation of thermal conductivity, revealing an extremely low lattice thermal conductivity of approximately 0.3−0.4 W/(m K) at 1223 K. The maximum zT of $Yb_{14}Mn_{1-x}Al_xSb_{11}$ is approximately 0.8 and 1.1 for the $x = 0$ and $x = 0.6$ compositions, respectively.

Introduction

Thermoelectric materials can directly convert waste heat from a variety of sources into electrical energy using the Seebeck effect.[1] The efficiency of a thermoelectric material is related to the dimensionless figure of merit (zT) given by eq 1

$$zT = \frac{a^2 T}{\rho\kappa} \quad (1)$$

where α is the Seebeck coefficient ($\Delta V/\Delta T$), T is temperature, ρ is electrical resistivity, and κ is thermal conductivity. Heavily doped semiconductors often have the best combination of Seebeck coefficient, resistivity, and thermal conductivity necessary for thermoelectric materials. However, high zT is difficult to achieve because these parameters are closely coupled and the enhancement of one is generally at the detriment of another. Recent strategies to improve thermoelectric materials have focused on lowering the lattice thermal conductivity, optimizing carrier concentration, and altering the density of states to enhance the Seebeck coefficient.[1−5]

Zintl phases are one class of materials where it might be possible to independently tune electrical and thermal properties to provide enhanced zT.[1,6] Zintl phases are valence precise compounds where there is complete charge transfer from the cation, typically a group 1 or 2 element, to the polyatomic anions, composed of group 13−15 elements.[7] A wide variety of structure types containing homo- or hetero polyanions (1, 2, or 3-dimensional), as well as discrete anions (0 D), have been synthesized and structurally characterized. The ability to tune properties has been demonstrated with a variety of materials such as clathrate structures,[8] skutterudite structures,[9] $Yb_{1-x}Ca_xZn_2Sb_2$,[10] and most recently, $Yb_{14}MnSb_{11}$.[3,11,12]

The discovery of high thermoelectric efficiency in *p*-type $Yb_{14}MnSb_{11}$ ($zT \approx 1$ at 1223 K) represents a significant advancement over the prior state of the art (*p*-type $Si_{0.8}Ge_{0.2}$ $zT \approx 0.6$).[11] $Yb_{14}MnSb_{11}$ is a rare-earth Zintl phase of the general formula $A_{14}MPn_{11}$ where A = alkaline earth, Yb, Eu cations; M = group 13 metalloid, Mn, Zn; and Pn = heavier group 15 element (P−Bi) and crystallizes in the $Ca_{14}AlSb_{11}$ structure type.[13] The structure of $A_{14}MPn_{11}$ is

* Corresponding author. E-mail: smkauzlarich@ucdavis.edu.
[†] Department of Chemistry, University of California.
[‡] California Institute of Technology.
[§] Peter A. Rock Thermochemistry Laboratory and NEAT ORU, University of California.
[||] Present address: Setram, Inc., 8430 Central Ave., Suite 3C and 3D, Newark, CA 94560.

(1) Snyder, G. J.; Toberer, E. S. *Nat. Mater.* **2008**, *7* (2), 105–114.
(2) Dresselhaus, M. S.; Chen, G.; Tang, M. Y.; Yang, R. G.; Lee, H.; Wang, D. Z.; Ren, Z. F.; Fleurial, J. P.; Gogna, P. *Adv. Mater.* **2007**, *19* (8), 1043–1053.
(3) Toberer, E. S.; Cox, C. A.; Brown, S. R.; Ikeda, T.; May, A. F.; Kauzlarich, S. M.; Snyder, G. J. *Adv. Funct. Mater.* **2008**, *18* (18), 2795–2800.
(4) Heremans, J. P.; Jovovic, V.; Toberer, E. S.; Saramat, A.; Kurosaki, K.; Charoenphakdee, A.; Yamanaka, S.; Snyder, G. J. *Science* **2008**, *321* (5888), 554–557.
(5) Bentien, A.; Christensen, M.; Bryan, J. D.; Sanchez, A.; Paschen, S.; Steglich, F.; Stucky, G. D.; Iversen, B. B. *Phys. Rev. B* **2004**, *69* (4), 045107.
(6) Kauzlarich, S. M.; Brown, S. R.; Snyder, G. J. *Dalton Trans.* **2007**, (21), 2099–2107.
(7) Kauzlarich, S. M., *Chemistry, Structure, and Bonding of Zintl Phases and Ions*; VCH Publishers: New York, 1996.
(8) Nolas, G. S.; Poon, J.; Kanatzidis, M. *MRS Bull.* **2006**, *31* (3), 199–205.
(9) Nolas, G. S.; Morelli, D. T.; Tritt, T. M. *Annu. Rev. Mater. Sci.* **1999**, *29*, 89–116.
(10) Gascoin, F.; Ottensmann, S.; Stark, D.; Haile, S. M.; Snyder, G. J. *Adv. Funct. Mater.* **2005**, *15* (11), 1860–1864.
(11) Brown, S. R.; Kauzlarich, S. M.; Gascoin, F.; Snyder, G. J. *Chem. Mater.* **2006**, *18* (7), 1873–1877.
(12) Brown, S. R.; Toberer, E. S.; Ikeda, T.; Cox, C. A.; Gascoin, F.; Kauzlarich, S. M.; Snyder, G. J. *Chem. Mater.* **2008**, *20* (10), 3412–3419.

10.1021/cm803252r CCC: $40.75
Published on Web 03/10/2009

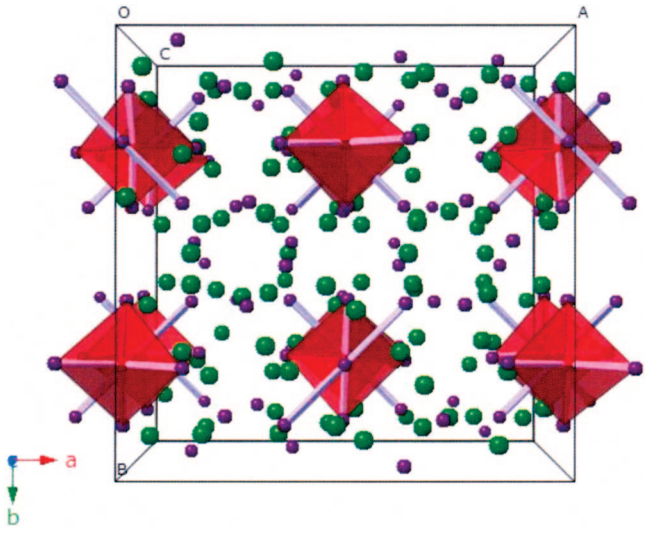

Figure 1. [001] view of the crystal structure for $Yb_{14}MSb_{11}$, showing the $[MSb_4]^{9-}$ tetrahedra, and Sb_3^{7-} linear rods. Yb^{2+} cations, Sb, and M atoms are shown in green, purple, and red, respectively.

shown in Figure 1; it contains A^{2+} cations, MPn_4^{9-} tetrahedral anions, Pn_3^{7-} linear anions, and isolated Pn^{3-} anions. Our initial investigations of improving $Yb_{14}MnSb_{11}$ through alloying suggest that the good thermoelectric properties can be further improved.[3,12] Alloying could target lowering the lattice thermal conductivity, optimizing the carrier concentration,[3] reducing the spin-disorder scattering,[12] or altering the band structure to enhance the Seebeck coefficient. The large unit cell, structural complexity, and variety of elements that can be substituted into this structure type[3,6,12−15] are particularly advantageous attributes. Substitution of trivalent Al for divalent Mn in $Yb_{14}MnSb_{11}$ leads to a reduced carrier concentration and thus an increased Seebeck coefficient and electrical resistivity. The optimum carrier concentration was found to occur at $x = 0.6-0.8$ in $Yb_{14}Mn_{1-x}Al_xSb_{11}$ and corresponds to a maximum zT of 1.3 at 1223 K (using the Dulong−Petit value for specific heat, discussed below).[3]

Thermal conductivity is calculated from the equation

$$\kappa_T = D_T d C_p \qquad (2)$$

where D_T is thermal diffusivity (measured), d is the bulk density of the sample, and C_p is the specific heat capacity at constant pressure. All prior work on the high temperature thermoelectric properties of $Yb_{14}MnSb_{11}$ has employed the Dulong−Petit law to approximate C_p.[3,11] The Dulong−Petit law is a classical value ($3k_B$/atom; 648.49 J/mol K for $Yb_{14}MnSb_{11}$) for the specific heat capacity of a harmonic crystal due to its lattice vibrations.[16] The specific heat at high temperatures typically exceeds the Dulong−Petit value primarily because of anharmonicity, as seen in thermoelectric SiGe alloys.[17]

Here, we report single crystal and powder X-ray diffraction data and microprobe characterization showing that the complete $Yb_{14}Mn_{1-x}Al_xSb_{11}$ solid solution can be prepared via flux synthesis. To more accurately assess the thermoelectric properties of these compounds, we have for the first time measured the specific heat from 300 to 1100 K for the $x = 0$, 0.2, and 0.6 compositions.

Experimental Section

Synthesis. $Yb_{14}Mn_{1-x}Al_xSb_{11}$ samples with $x = 0.2$, 0.4, 0.6, 0.8, and 0.95 were prepared by reacting the elements, Yb (sublimed dendritic pieces, 99.9%), Sb (shot, 99.9999%), Mn (pieces ground into powder, 99.98%), Al (shot, 99.9%) in a Sn (shot, 99.99+%) flux from Alfa Aesar. All materials were handled inside a nitrogen-filled drybox (water content <1.0 ppm). The elements, Yb:Mn:Al:Sb:Sn, were layered into 10 cm^3 Al_2O_3 crucibles in the ratios 14:11(1−x):11(x):11:86 where $x = 0.2$, 0.4, 0.6, 0.8, and 0.95. Excess (11 times) Mn and Al were used in order to prevent the formation of the binary phase $Yb_{11}Sb_{10}$. From here forth, all samples will be referred to by this synthetic x, designating the amount of Al loaded into the reactions. The samples were sealed in silica glass ampoules under vacuum. The reaction vessels were then heated from room temperature to 500 °C in 2 h, held at that temperature for 2 h, and then heated to 1000 °C in 2 h. They were held at 1000 °C for 6 h, and then cooled at 3 °C/h to 700 °C where the ampoules were inverted and centrifuged at 6500 rpm for 3−5 min to remove the molten Sn-flux from the crystals. After cooling, the reflective silver colored crystals were removed from the crucible inside a nitrogen-filled drybox equipped with a microscope for further analysis. The $x = 0$ and $x = 1$ samples were prepared according to published procedures.[18,19] For thermoelectric measurements, most of each sample was ground into a fine powder and then hot-pressed in high-density graphite dies (POCO) at about 20 000 psi and 1223 K for 1.5 h under argon, leading to sample density >95% of the theoretical density.

Single-Crystal X-ray Diffraction. In the drybox, small crystals were selected from each sample and transferred under paratone oil to a Bruker SMART 1000 CCD diffractometer utilizing a graphite-monochromatic Mo Kα radiation ($\lambda = 0.71069$ Å). A suitable crystal was positioned onto a glass fiber and placed under a cold nitrogen stream (90 K). Diffraction data were collected with the SMART software, and data reduction performed with SAINT version 6.45. Then, SADABS was used to apply a multiscan absorption correction. The initial atom positions were taken from previously published 14−1−11 structures,[20] and refined with SHELXTL version 5.1. Occupancies of the shared Mn and Al site were allowed to freely refine in order to determine the amount of Al in each sample. Refinement was also performed with Al/Mn occupancies equal to those found from the microprobe analysis; however, the thermal parameters were unreasonable so the freely refined occupancies are presented. The data collection, and unit-cell parameters are given in Table 1. Bond distances and angles for the $[MSb_4]^{-9}$ (M= Al, Mn) tetrahedron for the series are given in Table 2.

Electron Microprobe Analysis. Microprobe analysis was conducted on randomly selected crystals of each stoichiometry using a Cameca SX-100 Electron Probe Microanalyzer equipped with a

(13) Kauzlarich, S. M.; Payne, A. C.; Webb, D. J. *Magnetism: Molecules to Materials III*; Miller, J. S., Drillon, M., Eds.; Wiley-VCH: Weinheim, Germany, 2002; pp 37−62.
(14) Sales, B. C.; Jin, R.; Mandrus, D. *J. Phys. Soc. Jpn.* **2008**, *77* (Supplement A.), 48–53.
(15) Sales, B. C.; Khalifah, P.; Enck, T. P.; Nagler, E. J.; Sykora, R. E.; Jin, R.; Mandrus, D. *Phys. Rev. B* **2005**, *72* (20), 205207.
(16) Ott, J. B.; Boerio-Goates, J., *Chemical Thermodynamics: Principles and Applications*; Academic Press: London, 2000; p xxiii.
(17) Amano, T.; Beaudry, B. J.; Gschneidner, K. A.; Hartman, R.; Vining, C. B.; Alexander, C. A. *J. Appl. Phys.* **1987**, *62* (3), 819–823.
(18) Fisher, I. R.; Bud'ko, S. L.; Song, C.; Canfield, P. C.; Ozawa, T. C.; Kauzlarich, S. M. *Phys. Rev. Lett.* **2000**, *85* (5), 1120–1123.
(19) Fisher, I. R.; Wiener, T. A.; Bud'ko, S. L.; Canfield, P. C.; Chan, J. Y.; Kauzlarich, S. M. *Phys. Rev. B* **1999**, *59* (21), 13829–13834.
(20) Chan, J. Y.; Olmstead, M. M.; Kauzlarich, S. M.; Webb, D. J. *Chem. Mater.* **1998**, *10* (11), 3583–3588.

Table 1. Single-Crystal Data Collection Parameters for Each of the Crystals from the Reaction with Ideal Stoichiometry $Yb_{14}Mn_{1-x}Al_xSb_{11}$, where x = Reaction Stoichiometry

param	$x = 0.2$	$x = 0.4$	$x = 0.6$	$x = 0.8$	$x = 0.95$
experimental formula	$Yb_{14}Mn_{0.95(2)}Al_{0.05(2)}Sb_{11}$	$Yb_{14}Mn_{0.67(5)}Al_{0.33(5)}Sb_{11}$	$Yb_{14}Mn_{0.45(3)}Al_{0.55(3)}Sb_{11}$	$Yb_{14}Mn_{0.38(3)}Al_{0.62(3)}Sb_{11}$	$Yb_{14}Mn_{0.18(3)}Al_{0.82(3)}Sb_{11}$
cryst dimensions (mm^3)	0.1 × 0.03 × 0.08	0.08 × 0.06 × 0.4	0.32 × 0.22 × 0.2	0.2 × 0.12 × 0.14	0.36 × 0.3 × 0.28
space group	$I4_1/acd$	$I4_1/acd$	$I4_1/acd$	$I4_1/acd$	$I4_1/acd$
Z	8	8	8	8	8
T (K)	90	90	90	90	90
lattice params (Å)	$a = 16.588(2)$ $c = 21.910(4)$	$a = 16.583(2)$ $c = 21.985(4)$	$a = 16.586(2)$ $c = 22.041(4)$	$a = 16.585(2)$ $c = 22.046(4)$	$a = 16.585(2)$ $c = 22.082(4)$
cell volume ($Å^3$)	6028.8(17)	6045.9(17)	6063.3(17)	6063.8(17)	6074.2(17)
2θ range (deg)	4.92−59.16	4.92−51.00	4.92−60.00	4.92−60.00	4.92−60.00
no. of collected reflns	36 396	31 484	37 051	38 284	36 765
no. of unique reflns	2123	1418	2215	2214	2221
ρ_{calcd} (g cm^{-3})	8.407	8.366	8.329	8.324	8.297
μ Mo Kα (mm^{-1})	52.962	52.704	52.475	52.445	52.279
R1 [$I > 2\sigma(I)$][a]	0.0331	0.0452	0.0217	0.0258	0.0236
wR2	0.0613	0.1095	0.0602	0.0531	0.0593
largest diff peak and hole (e $Å^{-3}$)	3.041 and −3.049	4.376 and −4.028	3.005 and −1.870	2.268 and −2.133	3.542 and −2.192

[a] $R1 = [\Sigma||F_o| - |F_c||]/\Sigma|F_o|$; $wR2 = \{[\Sigma w[(F_o)^2 - (F_c)^2]^2]\}^{1/2}$; $w^1 = [\sigma^2(F_o) + (0.0471P)^2 + (0.5945P)]$ where $P = [\max(F_o^2,0) + 2F_c^2/3]$.

Table 2. Bond Lengths and Angles in the $[MSb_4]^{9-}$ tetrahedron (M = Mn, Al)

	M−Sb(2) Bond Length (Å)	Sb(2)−M−Sb(2) (deg)	Sb(2)−M−Sb(2)″ (deg)
$x = 0.2$	2.7429 (9)	105.566 (17)	117.60 (4)
$x = 0.4$	2.7325 (15)	105.93 (3)	116.80 (7)
$x = 0.6$	2.7245 (6)	106.132 (12)	116.38 (3)
$x = 0.8$	2.7213 (7)	106.197 (14)	116.24 (3)
$x = 0.95$	2.7104 (6)	106.388 (13)	115.83 (3)

wavelength-dispersive spectrometer with 20 kV accelerating potential and 10 nA beam current. The crystals were mounted with carbon tape onto 25 mm metal rounds. Net elemental intensities for Yb, Mn, Al, and Sb were determined with respect to pure elemental freshly polished calibration standards. There is peak-on-peak interference between the Yb Mα and Al Kα, however, the Al Kβ was too weak to be observed above the background, so the Al Kα had to be used. Measurements were taken to attempt to resolve the intensity of each peak despite the interference. The elemental composition was determined by taking 15−30 data points on multiple crystals of each stoichiometry, and then averages and standard deviations were calculated. Similar analysis was performed on the pellets formed after hot pressing for all samples except the $x = 0.2$ sample. Backscattered electron images of the pressed pellets, along with elemental maps for the $x = 0.6$ single crystal are provided in the Supporting Information.

Powder X-ray Diffraction. The hot-pressed pellets were polished inside the drybox with 30 μm alumina lapping film to remove surface oxidation, and then loaded into an air-sensitive sample holder. Powder X-ray diffraction data were collected at room temperature on a Bruker D8 Advance Diffractometer utilizing Cu Kα_1 radiation operated at 40kV and 40mA. Background subtraction and pattern analysis were performed using JADE 6.1 software.

Heat Capacity Measurements. Heat capacity of the single crystals, $x = 0$, 0.2, and 0.6, was measured between room temperature and 1100 K and was obtained utilizing a Setaram Sensys calorimeter operated in a step mode. Alumina powder (Aldrich, 99.99%), dried and stabilized in the corundum phase by heating overnight at 1773 K, was used as a calibrant. The errors in heat capacity were estimated by running TiO_2 (99.999%, Sigma-Aldrich) and ZrO_2 (99.978%, Alfa-Aesar) standards and comparing them with tabulated data.[21]

A collection of crystals with composition $x = 0$, 0.2, and 0.6 were ground into powder of approximately 0.380−0.460 g. The estimated accuracy in heat capacity is 2−5% with the highest error at high temperature. All measurements were carried out by continuous heating steps of 10 K/min and 20 min isothermal holds between $T = 300$ and 1100 K in the heating direction. The signal was collected about every 30 K. The amount of residual Sn flux was calculated from the endotherm for Sn melting ($T = 505$ K) and was found to be 4.3, 10.8, and 1.8 wt % for the $x = 0$, 0.2, and 0.6 samples, respectively, using a melting enthalpy of 107.5 J/g. The melting enthalpy of the residual Sn-flux occurred over 1−3 data points because of the narrow melting peak and those points were removed. The heat capacity was corrected for the appropriate amount of Sn, taken from the thermodynamic database.[21]

Thermogravimetric/differential scanning calorimetry (TG/DSC) was performed up to 1073 K on the hot pressed pellets with a Netzsch Thermal Analysis STA 409 instrument. The data indicate that the sample does not melt or have any phase transitions up to 1400 K. The majority of the residual Sn is released during the hot-pressing process, so only a very small amount of Sn was observed in the DSC data from the pressed pellets, ranging from 0.25−0.65% by mass.

Transport Properties. Data for the thermal diffusivity, Seebeck coefficient and electrical resistivity were taken from previous work.[3] A single linear fit (combining all samples) to the experimentally obtained high temperature heat capacity was used for the calculations of thermal conductivity (eq 2) and zT (eq 1).

Results and Discussion

Single-Crystal Structure. A high yield of crystals was obtained for all samples from a Sn flux. Several crystals were chosen and screened with single crystal X-ray diffraction for a unit cell refinement. One crystal from each composition was chosen for a full data collection and structural refinement. Table 1 shows the crystallographic refinement parameters. The structure of each compound refined well in the $I4_1/acd$ space group with R1 < 0.05. The refinement of the structures indicated that there was less Al in the structure than the synthetic amount, x, used when filling the reaction vessels. The lattice parameter a remains virtually unchanged with increasing Al (16.588 (2) Å for $x = 0.2$ to 16.585 (2) Å for $x = 0.95$). However, c increases by approximately 0.17 Å from 21.910 (4) to 22.082 (4) Å. This increase in the c lattice parameter is approximately linear with the experimentally determined Al content. The volume increases linearly with increasing Al.

(21) *FactSage 5.3*; Thermfact/CRCT and GTT-Technologies: Montreal, QB, and Aachen, Germany, 2003.

The structure type has been described in detail before and the main points of the structural refinement will only be briefly commented on herein.[20] The structural unit that might be expected to be most affected by the Al substitution is the $[MSb_4]^{9-}$ tetrahedron (−4 site symmetry) containing a mixture of Mn and Al. Bond lengths and angles all changed slightly but regularly with increasing Al content. Only the tetrahedral bond lengths and angles are reported in Table 2 because that is the only site in which the composition is changing. The increase in the *c* axis cannot be attributed to an increase in the M−Sb bond length because, as Table 2 shows, the M−Sb bond decreases slightly from 2.7429 (9) to 2.7104 (6) Å as the Al content increases. This decrease is expected because the ionic radius of Al^{3+} (0.39 Å) is smaller than the ionic radius of Mn^{2+} (0.66 Å).[22] The bond angles of the tetrahedron also vary with increasing Al content, moving toward the ideal geometry, 109.5°. The increase in angle from 105.566 (17) and 117.60 (4)° for $x = 0.2$ to 106.388 (13) and 115.83 (3)° for $x = 0.95$ is the main reason for the increasing volume. As the angle increases toward the ideal value of 109.5°, the *c* axis is the most affected and the overall volume increases. The change in angle, i.e., the Sb−M−Sb bond angle becoming more ideal as more Al is added, can be attributed to either steric or electronic effects and steric effects appear to be unlikely. In many of our papers on the Mn-containing analogs, we attributed the distortion of the Mn tetrahedron to a Jahn−Teller distortion (Mn^{3+}), which provided a consistent interpretation of the observed magnetic moment of 4 unpaired spins in the paramagnetic and the ordered regime.[13,19,23] More recent X-ray magnetic circular dichroism (XMCD)[24] and XPS[25] data for $Yb_{14}MnSb_{11}$ indicate that Mn is in a 2+ oxidation state. This requires an additional hole (h^+) per formula unit in the formal charge distribution for the tetrahedral cluster: $[Mn^{2+}Sb_4^{12-} + h^+]^{9-}$ vs $[Al^{3+}Sb_4^{12-}]^{9-}$. The observed metallic conduction (increasing resistivity with increasing temperature) of $Yb_{14}MnSb_{11}$ indicates the hole is delocalized throughout the structure and therefore not entirely on the tetrahedral cluster. The hole is spin-polarized, giving rise to a total moment of 4 unpaired electrons per formula unit.[26] XMCD results[24] point to the delocalized hole having primarily Sb 5p character. Mn d hybridization with the Sb states near the Fermi level would enable the Jahn−Teller effect for the cluster, $[Mn^{2+}Sb_4^{12-} + h^+]^{9-}$, as the presence of a hole leaves a degenerate state partially filled. The $[Al^{3+}Sb_4^{-12}]^{9-}$ tetrahedron would not exhibit a Jahn−Teller effect, thus the distortion in the Sb−M−Sb bond angle diminishes as more Al is added.

Table 3. Calculated Compositional Formula from Electron Microprobe on Single Crystals and Pressed Pellets (data for the $x = 0.2$ pressed pellet was not obtained)

synthetic x = Al	formula from electron microprobe	
	single crystals	pressed pellets
$x = 0.2$	$Yb_{13.8(1)}Mn_{1.06(2)}Al_{0.13(4)}Sb_{11.0(1)}$	
$x = 0.4$	$Yb_{13.84(13)}Mn_{0.76(4)}Al_{0.46(8)}Sb_{10.95(15)}$	$Yb_{13.67(6)}Mn_{0.74(2)}Al_{0.41(8)}Sb_{11.18(6)}$
$x = 0.6$	$Yb_{13.70(7)}Mn_{0.54(6)}Al_{0.63(6)}Sb_{11.13(8)}$	$Yb_{13.78(7)}Mn_{0.61(2)}Al_{0.56(3)}Sb_{11.06(8)}$
$x = 0.8$	$Yb_{13.67(23)}Mn_{0.40(5)}Al_{0.76(8)}Sb_{11.17(27)}$	$Yb_{13.78(6)}Mn_{0.33(2)}Al_{0.82(3)}Sb_{11.08(5)}$
$x = 0.95$	$Yb_{13.77(9)}Mn_{0.19(2)}Al_{0.98(3)}Sb_{11.06(11)}$	$Yb_{13.78(7)}Mn_{0.14(1)}Al_{0.99(4)}Sb_{11.08(7)}$

The $Yb_{14}Mn_{1-x}Al_xSb_{11}$ single-crystal samples were found to be homogeneous by electron microprobe. The electron-microprobe analysis for the single crystals and pressed pellets is provided in Table 3 and is consistent with the single-crystal data for the amount of Mn and Al in each sample. Microprobe measurements were consistently higher for Al and lower for Yb than single-crystal measurements, but were within reasonable experimental error. This is illustrated in Figure 2a where the synthetic *x* value is compared to the experimentally determined value for single-crystal X-ray diffraction and electron microprobe. For this series of compounds, microprobe is less reliable than single-crystal analysis because there is interference between Al Kα and Yb Mα emission. The result of this interference is that some of the intensity of the Yb peak contributes to the Al peak

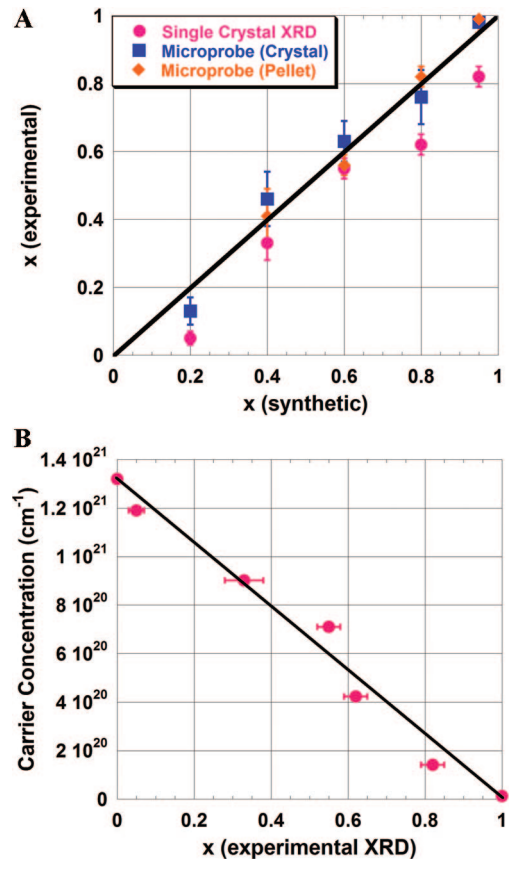

Figure 2. (A) Comparison of the nominal value of x = Al content to the experimentally determined value of x found from electron microprobe analysis and single-crystal X-ray diffraction. The black line connects $x = 0$ and $x = 1$ in order to show the expected correlation of x(synthetic) = x(experimental). (B) Carrier concentration as a function of the experimentally determined value of x from single-crystal X-ray diffraction. The black line connects the $x = 0$ and $x = 1$ in order to show the expected correlation between stoichiometry and carrier concentration.

(22) Giacovazzo, C.; Monaco, H. L.; Viterbo, D.; Scordari, F.; Gilli, G.; Zanotti, G.; Catti, M., *Fundamentals of Crystallography*; IUCr-Oxford University Press: New York, 1992; p 654.
(23) Kauzlarich, S. M.; Kuromoto, T. Y.; Olmstead, M. M. *J. Am. Chem. Soc.* **1989**, *111* (20), 8041–8042.
(24) Holm, A. P.; Kauzlarich, S. M.; Morton, S. A.; Waddill, G. D.; Pickett, W. E.; Tobin, J. G. *J. Am. Chem. Soc.* **2002**, *124* (33), 9894–9898.
(25) Holm, A. P.; Ozawa, T. C.; Kauzarich, S. M.; Morton, S. A.; Waddill, G. D.; Tobin, J. G. *J. Solid State Chem.* **2005**, *178* (1), 262–269.
(26) Sanchez-Portal, D.; Martin, R. M.; Kauzlarich, S. M.; Pickett, W. E. *Phys. Rev. B* **2002**, *65* (14), 144414.

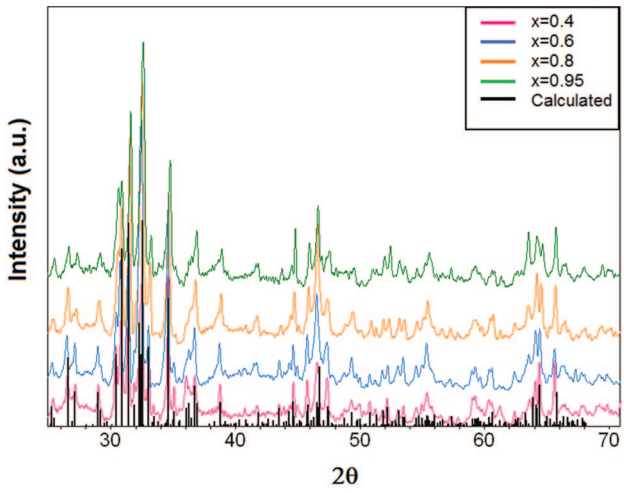

Figure 3. Powder X-ray diffraction patterns for $Yb_{14}Mn_{1-x}Al_xSb_{11}$. The calculated pattern is for $x = 0$. The intensity is offset for clearer viewing.

Table 4. Lattice Parameters from Powder X-ray Diffraction

	powder X-ray refinement of pressed pellets at 300 K	
synthetic x	lattice a (Å)	lattice c (Å)
$x = 0.2$		
$x = 0.4$	16.582 (3)	21.989 (6)
$x = 0.6$	16.585 (3)	22.037 (9)
$x = 0.8$	16.581 (4)	22.045 (8)
$x = 0.95$	16.586 (3)	22.083 (7)

giving rise to slightly lower Yb and higher Al when compared to single crystal data. The differences in composition are small and within standard deviation, so the synthetic x value for each composition is used throughout. We have previously shown that this value is consistent with the carrier concentration.[3] With these stoichiometry values, the consistency between composition and carrier concentration is better (Figure 2b). The black lines in panels a and b in Figure 2 are to help guide the eye as to the expected correlation. Phase purity and homogeneity of the hot-pressed pellets were characterized with X-ray powder diffraction and back scattered electron (BSE) images. The powder patterns, for $x =$ 0.4, 0.6, 0.8, and 0.95 of the hot-pressed pellets are shown in Figure 3. These diffraction patterns match well with the calculated powder pattern for $Yb_{14}MnSb_{11}$, indicating phase purity. Refined lattice parameters obtained from the data agree with those from single-crystal X-ray data (Table 4). The BSE images (Supporting Information) are also consistent with single-phase, hot-pressed pellets.

Heat Capacity Measurements. Figure 4 shows the molar heat capacity as a function of temperature, along with the average of the three samples, which are within 5% error. The heat capacity in this study was measured well above the Debye temperature of the samples (estimated to be 160 $\pm$ 10 K in $Yb_{14}MnSb_{11}$)[19] and could be extrapolated to higher temperatures by a linear function. The linear fit of the average, $C_p = 0.0898T + 663.49$ J/(mol K) ($R^2 = 0.60$), shown in Figure 4, was used for thermal conductivity calculations. For the $x = 0$ sample only, the fit becomes significantly better ($R^2 = 0.90$). The noise and poor correlation in the $x = 0.6$ and $x = 0.2$ samples is attributed to poor thermal contact with the crucible.

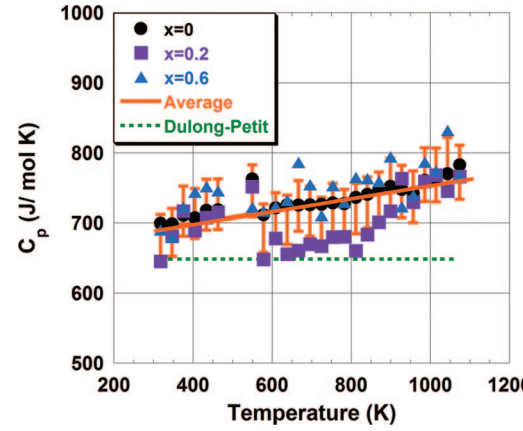

Figure 4. Molar heat capacity for three flux-grown samples as a function of temperature corrected for residual Sn; the average is shown with 5% error bars.

Within the measurement limitations, the heat capacity is found to be independent of composition. This is consistent with binary alloys such as $Mn_{1-x}Al_xSb$, where the heat capacity can be calculated via the Newman-Koop rule, from the heat capacity of the end members, MnSb and AlSb.[21] Calculated heat capacities of the binary alloy $Mn_{1-x}Al_xSb$, $x = 0.6$, showed only a 0.5% change in the heat capacity at 298 K (1% at 1200 K). Likewise, studies of SiGe alloys reveal the heat capacity is independent of alloy composition.[27]

The heat capacity of a solid is typically dominated by the phonon contribution. For a harmonic crystal, the phonon specific heat rises with temperature below the Debye temperature, Θ_D (160 $\pm$ 10 K for $Yb_{14}MnSb_{11}$),[19] and then approaches the Dulong−Petit value. At high temperatures ($T \gg \Theta_D$) any anharmonic potential of the atoms leads to thermal expansion, nonzero Grüneisen parameter and an increase in heat capacity above the Dulong−Petit value ($C_{DP} = 3k_B$/atom).[28] The change in volume induced from the thermal expansion leads to a difference in the specific heat capacity at constant volume (C_v) and that at constant pressure (C_p) with $C_p > C_v$. The lowest order anharmonic addition to the heat capacity increases linearly with temperature.[29]

The electronic heat capacity also increases linearly with temperature and can be significant in metals at high temperature.[28] This electronic specific heat (which should depend on the carrier concentration and therefore x in $Yb_{14}Mn_{1-x}Al_xSb_{11}$) should remain linear with temperature as long as the electrons remain degenerate, up to about half of the classical limit where it saturates: $3k_B/2$ per electron.[30] There is no indication of reaching nondegenerate electrons even at 1275 K in $Yb_{14}MnSb_{11}$ because both the C_p and Seebeck coefficient increase linearly with temperature as expected for degenerate electrons. The linear term in C_p for $Yb_{14}MnSb_{11}$ measured at low temperatures is as large or larger (0.16 J/(mol K^2)[15] or 0.07 J/(mol K^2) [19]) than that measured here (0.09 J/(mol K^2)). This and the lack of a clear trend in the

(27) Gerlich, D.; Abeles, B.; Miller, R. E. *J. Appl. Phys.* **1965**, *36* (1), 76–79.
(28) Foreman, A. J. E. *Proc. Phys. Soc. London* **1962**, *79* (512), 1124–1141.
(29) Enck, F. D. *Phys. Rev.* **1960**, *1* (6), 1873–1877.
(30) Mott, N. F.; Jones, H. *The Theory of the Properties of Metals and Alloys*; Dover: New York, 1936.

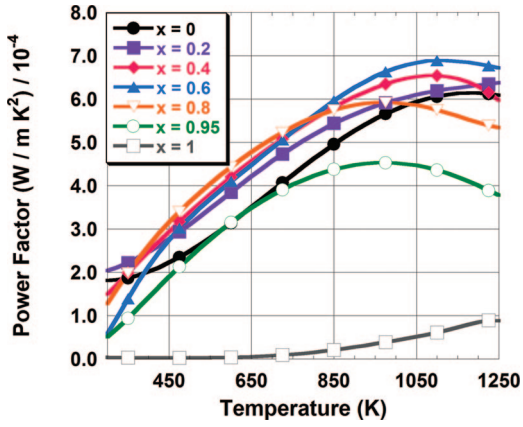

Figure 5. Power factor versus temperature of the $Yb_{14}Mn_{1-x}Al_xSb_{11}$ series. Compounds with $x > 0.6$ show reduction in the power factor because of a compensated Seebeck coefficient.

magnitude of the temperature dependence of C_p with x suggests that the electronic term may be smaller than the resolution of the measurement.

The high-temperature heat capacity in Si, Ge, and SiGe alloys has been represented by $C_p/C_{DP} = aT/\Theta_D + b$, where $a = 0.081$ and $b = 0.95$ is independent of the alloy composition.[27] Drop calorimetry data on thermoelectric SiGe alloys confirmed this behavior but with a and b values 3−7% smaller.[17] From the experimental work reported here, we find values of $a = 0.022$ and $b = 1.02$ using a Θ_D of 160 K.

Thermal Conductivity and *zT*. The temperature-dependent Seebeck and resistivity have been previously reported and the power factor (α^2/ρ) is shown in Figure 5.[3] Decreasing carrier concentration leads to increases in both the electrical resistivity and Seebeck coefficients, with an optimum carrier concentration of $4-6 \times 10^{20}$ holes/cm^3 corresponding to an $x = 0.6-0.8$.[3] The largest power factors occur at higher carrier concentrations than the peak in zT because of the exceptionally low lattice thermal conductivity.[1] The thermal conductivity of this series has been previously reported,[3] and here it is re-evaluated using the linear fit of the average C_p. The total, κ_T, and lattice, κ_l, thermal conductivity are shown using polynomial functions in Figure 6. Even with this revised thermal conductivity, this is still a low thermal conductivity material, with κ_l as low as Zn_4Sb_3.[1,31] This fits the description of a electron crystal phonon glass model necessary for high zT materials.[31] Because the C_p increases with temperature, these values of κ_T are on average 7% higher at room temperature and 19% higher at 1223 K than those previously reported.[3] This large deviation at higher temperatures leads to a decrease in maximum zT, shown in Figure 7. The parent material, $Yb_{14}MnSb_{11}$, reaches a maximum zT near 0.8 at 1223 K. The Al-doped series reaches a maximum near 1.1 for the $x = 0.6$ sample near 1223 K, followed closely by the $x = 0.8$ sample. This reduction in zT is the same as the increase in thermal conductivity, approximately 19%. For exploratory research, the Dulong-Petit value provides a starting point for estimating heat capacity, but it should be recognized that it can lead to an overestimation of zT.

(31) Snyder, G. J.; Christensen, M.; Nishibori, E.; Caillat, T.; Iversen, B. B. *Nat. Mater.* **2004**, *3* (7), 458–463.

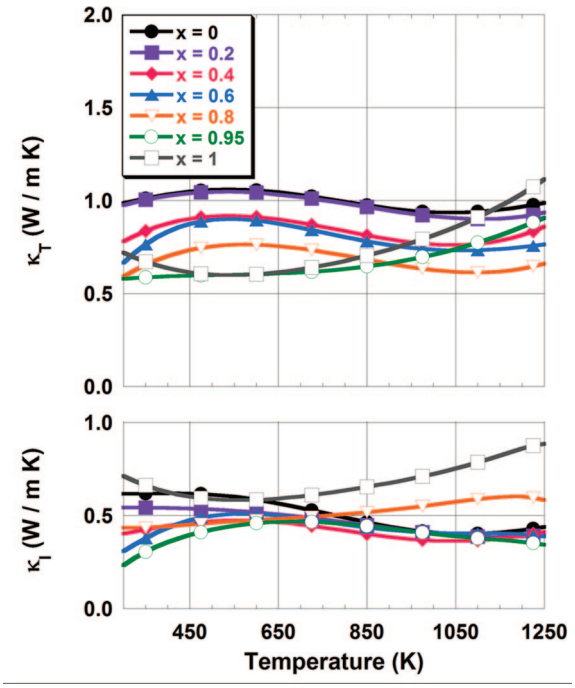

Figure 6. Total thermal conductivity (κ_T) and lattice thermal conductivity (κ_l) versus temperature of the $Yb_{14}Mn_{1-x}Al_xSb_{11}$ series calculated with the experimentally determined heat capacity.

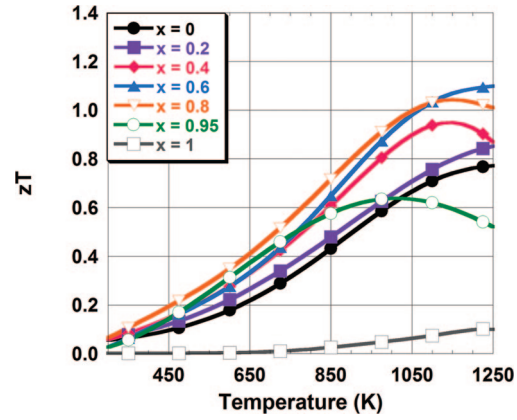

Figure 7. The zT versus temperature of $Yb_{14}Mn_{1-x}Al_xSb_{11}$ reaches a maximum of approximately 1.1 for the $x = 0.6$. For the $x = 0$, the maximum zT is 0.8.

Conclusion

The solid solution, $Yb_{14}Mn_{1-x}Al_xSb_{11}$, can be made via a Sn flux route. Characterization by electron microprobe analysis and single-crystal X-ray diffraction are consistent with Al being incorporated into the structure near the intended value, x. Heat capacity measurements indicate that the heat capacity for these materials is independent of composition, but linearly temperature dependent. The experimentally determined heat capacity, C_p, is 7−19% higher in the 300−1223 K temperature range compared to the Dulong−Petit value. The measured high temperature heat capacity permits a recalculation of zT, yielding a peak zT value of 1.1 for the $x = 0.6$ composition.

Acknowledgment. Financial support from NSF DMR-0600742, the NASA Jet Propulsion Laboratory, the Beckman Foundation, and NSF DMR 06−01892 (calorimetry) is grate-

fully acknowledged. C.C. acknowledges a NSF funded LSAMP Bridge to the Doctorate Fellowship. We thank Christine Beavers, Marilyn M. Olmstead, and Håkon Hope for useful discussion.

Supporting Information Available: X-ray crystallographic data for the single-crystal refinement of $Yb_{14}Mn_{1-x}Al_xSb_{11}$ ($x = 0.2$, 0.4, 0.6, 0.8, and 0.95) (TXT). Backscattered electron and elemental mapping images of the pressed pellets and single crystal ($x = 6$), respectively (PDF). This material is available free of charge via the Internet at http://pubs.acs.org.

CM803252R